Article

Vascular and Metabolic Responses to Elevated Circulating PDGF-BB in Mice: A Multiparametric MRI Study

Xiuli Yang [1,†], Jiekang Wang [2,3,†], Yuguo Li [1,4], Mei Wan [2,3,*], Zhiliang Wei [1,4,*]

[1] Russell H. Morgan Department of Radiology and Radiological Science, Johns Hopkins University School of Medicine, Baltimore, MD 21205, USA
[2] Department of Orthopaedic Surgery, Johns Hopkins University School of Medicine, Baltimore, MD 21205, USA
[3] Department of Biomedical Engineering, Johns Hopkins University School of Medicine, Baltimore, MD 21205, USA
[4] F. M. Kirby Research Center for Functional Brain Imaging, Kennedy Krieger Research Institute, Baltimore, MD 21205, USA
* Correspondence: mwan4@jhmi.edu (M.W.); zhiliang.wei@jhu.edu (Z.W.)
† These authors contributed equally to this work.
Received: 20 November 2024; Revised: 20 December 2024; Accepted: 22 January 2025; Published: 2 April 2025

Abstract: Elevated circulating platelet-derived growth factor-BB (PDGF-BB) has been implicated in the development of various aged-related pathologies and is recognized as a potential pro-aging factor. Although numerous studies have explored the pathological roles of the PDGF-BB/PDGFRβ signaling pathway, few investigations have dissected its function in neurofunctional responses to elevated circulating PDGF-BB, primarily because in-vivo measurements are generally required to assess neurofunction. To address this knowledge gap, we characterized the vascular and metabolic responses to elevated circulating PDGF-BB in vivo using multiparametric non-invasive non-contrast MRI techniques in a conditional *Pdgfb* transgenic mouse model ($Pdgfb^{cTG}$) at 6 months of age. Results indicated that $Pdgfb^{cTG}$ mice exhibited decreased cerebral blood flow ($p = 0.025$), elevated oxygen extraction ($p = 0.002$), and increased metabolic rate of oxygen ($p = 0.035$), mirroring the changes observed in human aging. The rate of change in vascular and metabolic measurements in the model mice was significantly higher (≥200.3%) compared to that of naturally aged mice. This study provides neurofunctional evidence that elevated circulating PDGF-BB accelerates neurovascular aging.

Keywords: PDGF-BB; cerebral blood flow; oxygen extraction fraction; cerebral metabolic rate of oxygen; relaxation time; diffusion

1. Introduction

Platelet-derived growth factor-BB (PDGF-BB) is increasingly recognized as a key factor driving age-related pathologies, including brain aging [1,2]. In physiological conditions, PDGF-BB promotes the proliferation and migration of cells during wound healing and tissue regeneration [3]. The PDGF-BB/PDGFRβ signaling pathway mediates the crosstalk between pericytes and endothelial cells, playing an important role in the establishment and maintenance of pericyte coverage on cerebral microvasculature [4,5]. Clinical data have shown elevated levels of soluble PDGFRβ, a marker of pericyte degeneration, in the cerebrospinal fluid of patients with mild cognitive impairment and Alzheimer's disease (AD) [6,7], suggesting that dysregulation of the PDGF-BB/PDGFRβ signaling pathway is associated with disease development.

The serum/plasma PDGF-BB concentrations in aged mice and humans have been shown to be increased by 2–3 folds compared to their young controls [1,2,8]. Skeletal $TRAP^+$ preosteoclast-secreted PDGF-BB is a major contributes to the pathological elevation of circulating PDGF-BB, promoting arterial stiffening [1] and calcification during aging [2]. Persistently high PDGF-BB levels induce pericyte loss in the brain by enhancing enzymatic shedding of its receptor, PDGFRβ, from the pericyte membrane. This inhibits the PDGF-BB/PDGFRβ signaling, causes blood-brain barrier (BBB) leakage [8]. In addition to these vascular impairments, a recent study on humans found that circulating PDGF-BB levels were associated with white-matter dysfunction [9], a known risk factor for adverse neurovascular aging.

Understanding the dual role of PDGF-BB as both a necessary growth factor and a potential pro-aging agent is crucial for developing future therapies aimed at mitigating aging and halting age-related neurodegenerative

diseases, such as AD or vascular dementia [10–12]. To further investigate the impact of elevated circulating PDGF-BB on brain neurofunction, we aimed to characterize the vascular and metabolic responses using a transgenic $Pdgfb^{cTG}$ model [8,13] that overexpresses *Pdgfb*. A multiparametric MRI study, combined with immunofluorescence analysis of brain tissue sections, was conducted to explore the neurofunctional profile of the $Pdgfb^{cTG}$ mouse model.

2. Material and Methods

2.1. General Procedures

The experimental protocols for this study were approved by the Johns Hopkins Medical Institution Animal Care and Use Committee and conducted in accordance with the National Institutes of Health guidelines for the care and use of laboratory animals. Data reporting complied with the ARRIVE 2.0 guidelines. A cohort of 5 $Pdgfb^{cTG}$ mice (age: 6 months; body weight: 29–35 g; males) and 5 littermate wild-type (WT) controls (age: 6 months; body weight: 26–34 g; males) was used in this study. No significant difference in body weight was observed between the WT and $Pdgfb^{cTG}$ mice (unpaired *t*-test: degree of freedom = 8, $t = 2.07$, $p = 0.072$). All mice were housed in a quiet environment controlled to a 12-h day/night cycle and had ad libitum access to food and water.

The experimenter who performed the MRI scans was blinded to the group assignments. Mice were scanned randomly using a previously reported scheme [14]. Briefly, mice were assigned consecutive numbers starting from one. A set of pseudorandom numbers was generated using the MATLAB (MathWorks, Natick, MA, USA) "rand" function, and the ranks of these numbers (from largest to smallest) determined the experimental order. For instance, if the first pseudorandom number ranked third, the mouse preassigned to number 3 was the first to be scanned.

2.2. Multiparametric MRI Experiments

All MRI experiments were performed on an 11.7T Bruker Biospec system (Bruker, Ettlingen, Germany) with a horizontal bore and an actively shielded pulse field gradient (maximum intensity of 0.74 T/m). Images were acquired using a 72-mm quadrature volume resonator as the transmitter, and a four-element (2 × 2) phased-array coil as the receiver. Magnetic field homogeneity over the mouse brain was optimized using global shimming (up to the second order) based on a pre-acquired subject-specific field map. To minimize stress and motion in the mice, inhalational isoflurane was delivered with medical air (21% O_2 and 78% N_2) at a flow rate of 0.75 L/min. Anesthesia induction was achieved with 1.5–2.0% isoflurane for 15 min. At the 10th min under induction, the mouse was placed onto a water-heated animal bed with temperature control and positioned with a bite bar, a pair of ear pins, and a custom-built 3D-printed holder before entering the magnet. After induction, the isoflurane concentration was reduced to 1.0% for maintenance during the MRI scans.

Each mouse underwent a set of MRI scans as described in Figure 1, which included the fast spin echo (FSE) MRI to measure brain volume, phase-contrast (PC) for global cerebral blood flow (gCBF), pseudo-continuous arterial spin labeling (pCASL) for regional cerebral blood flow (rCBF), T_2-relaxation-under-spin-tagging (TRUST) for oxygen extraction fraction (OEF), and diffusion-weighted imaging (DWI) for apparent diffusion coefficient (ADC) [15–18]. Cerebral metabolic rate of oxygen ($CMRO_2$) was calculated using the Fick principle [19].

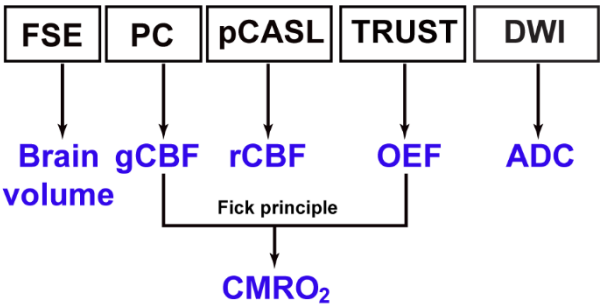

Figure 1. Schematic diagram of MRI scans. A set of multiparametric MRI techniques was utilized, including fast spin echo (FSE) for assessing brain volume, phase-contrast (PC) for gCBF, pseudo-continuous arterial spin labeling (pCASL) for rCBF, T_2-relaxation-under-spin-tagging (TRUST) for OEF, and diffusion-weighted imaging (DWI) for ADC. $CMRO_2$ was calculated based on gCBF and OEF using the Fick principle.

The parameters for the T_2-weighted FSE MRI were as follows: repetition time (TR)/echo time (TE) = 4000/10.0 ms, field of view (FOV) = 15 mm [rostral-caudal] × 15 mm [left-right], matrix size = 128 × 128, slice thickness = 0.5 mm (without inter-slice gap), echo spacing = 5.0 ms (4 spin echoes per scan), 35 axial slices, and scan duration = 2.1 min [14].

The PC MRI scanning covered the four major feeding arteries: left internal carotid artery (LICA), right internal carotid artery (RICA), left vertebral artery (LVA), and right vertebral artery (RVA), in separate scans to obtain corresponding through-plane velocity maps [16]. Prior to the PC scans, a coronal time-of-flight (TOF) angiogram was performed (TR/TE = 45/2.6 ms, FOV = 25 mm × 16 mm, matrix size = 256 × 256, 9 slices without inter-slice gap, slice thickness = 0.5 mm, scan duration = 2.6 min) to visualize the feeding arteries. Next, a sagittal TOF (TR/TE = 60/2.5 ms, FOV = 16 mm × 16 mm, matrix size = 256 × 256, single slice tilted to cover the targeted artery identified from the coronal TOF images, slice thickness = 0.5 mm, scan duration = 0.4 min) was applied to visualize the in-plane trajectory of the targeted artery. Based on the reference TOF images (coronal and sagittal), the PC MRI was positioned and performed using the following parameters: TR/TE = 15/3.2 ms, FOV = 15 mm × 15 mm, matrix size = 300 × 300, slice thickness = 0.5 mm, average number = 4, dummy scan = 8, receiver bandwidth = 100 kHz, flip angle = 25°, encoding velocity = 20 (for LICA/RICA)/10 (for LVA/RVA) cm/s, partial Fourier acquisition factor = 0.7, and scan duration = 0.6 min per artery [16].

A two-scan pCASL method, which was designed to minimize the influence of magnetic-field inhomogeneity, was utilized [18,20]. First, a pre-scan was performed to optimize the phases of the labeling pulses in both the control and labeled scans. Subsequently, the scan focusing on regional perfusion was performed with the following parameters [21,22]: TR/TE = 3000/13.1 ms, labeling duration = 1800 ms, FOV = 15 mm × 15 mm, matrix size = 96 × 96, slice thickness = 0.75 mm, labeling-pulse width = 0.4 ms, inter-labeling-pulse delay = 0.8 ms, flip angle of labeling pulse = 40°, post-labeling delay = 300 ms, two-segment spin-echo echo-planar imaging (EPI) acquisition, partial Fourier acquisition factor = 0.7, number of average = 25, and scan duration = 5.0 min.

TRUST MRI was performed on the confluence of sinuses using the following procedure [17,23]. To visualize the confluence of sagittal sinuses, an axial TOF scan was first performed under TR/TE = 20/2.7 ms, FOV = 15 mm × 15 mm, matrix size = 256 × 256, 5 axial slices, slice thickness = 0.5 mm, and scan duration = 0.3 min. The TRUST scan followed the reported protocol [17,24]: TR/TE = 3500/6.5 ms, FOV = 16 mm × 16 mm, matrix size = 128 × 128, slice thickness = 0.5 mm, EPI factor = 16, inversion-slab thickness = 2.5 mm, post-labeling delay = 1000 ms, eTE = 0.3, 20, 40 ms, echo spacing of eTE = 5.0 ms, 3 repetitions, and scan duration = 8.4 min.

Key parameters of DWI MRI were: TR/TE = 2500/18.0 ms, FOV = 15 mm × 15 mm, matrix size = 128 × 128, slice thickness = 0.75 mm, encoding direction = 6, b = 650 s/mm^2, receiver bandwidth = 300 kHz, 20 axial slices, and scan duration = 4.5 min with 4-segment spin-echo EPI acquisition.

Vital physical signs of respiration rate and heart rate were recorded. Respiration rate was monitored using a MR-compatible system (SA Instruments, Stony Brook, USA). Heart rate was measured non-invasively (to avoid potential physiological perturbation due to electrocardiogram needle penetrations) using an ultra-short-evolution-time (UTE) MRI sequence. This sequence repeatedly acquired the center *k*-space to generate a time course of MR signal intensity that reflected the R-R interval. The experimental parameters were as follows [25]: TR/TE = 8/0.3 ms, FOV = 25 mm × 25 mm, matrix size = 96 × 96, slice thickness = 3.0 mm, and scan duration = 0.4 min. An axial imaging slice was positioned over the heart with reference to a scout image targeting the abdomen.

At the end of the MRI sessions, blood samples (one or two drops) were collected from each mouse using the submandibular bleeding method, and hemoglobin levels were measured with a HemoCue device.

2.3. Immunofluorescent Staining of Brain Tissue Sections

Brain sections were collected and processed following a previously described protocol [2,8]. Briefly, mice were perfused transcardially with PBS, followed by phosphate-buffered 4% paraformaldehyde. The brains were fixed in phosphate-buffered 4% paraformaldehyde for 24 h at 4 °C, divided into two hemispheres from the midsagittal line, and dehydrated with 30% sucrose. Frozen brain tissue sections at the thickness of 50 μm were prepared using a cryostat. After blocking and antigen retrieval procedures, the brain sections were incubated with primary antibodies for 3 days at 4 °C. Subsequently, sections were incubated overnight with matched fluorescence-linked secondary antibodies (Jackson ImmunoResearch Laboratories, West Grove, USA). The primary antibodies used were CD13 (1:200, MCA2183, Bio-Rad, Hercules, USA) and CD31 (1:200, FAB3628G, R&D Systems, Minneapolis, USA). Fluorescent-tagged images were scanned using a confocal microscope (Zeiss LSM780 FCS, Oberkochen, Germany; Leica SP5, Wetzlar, Germany).

2.4. Data Processing

Custom-written MATLAB scripts and graphic-user-interface tools were used following the procedures described briefly below.

For PC MRI, the artery of interest was first manually delineated on the complex-difference image, which showed excellent contrast between the vessel and surrounding tissue [16]. The mask was then applied to the velocity map, and the integration of arterial voxels yielded blood flow through the artery in ml/min. The total blood flow to the brain was calculated by summing the blood flow values across the four major feeding arteries. To account for brain-size differences and obtain unit-mass CBF values, the total blood flow was divided by the brain weight, calculated as the product of brain volume and tissue density (1.04 g/mL) [26]. The gCBF value was reported as milliliters per 100 g of brain tissue/min (ml/100 g/min).

The processing of pCASL data followed established procedures [14]. Pair-wise subtraction between control and labeled images (i.e., $M_{ctr} - M_{lbl}$) was first performed to yield a difference image, which was then divided by an M_0 image (obtained by scaling the control image [18]) to provide a perfusion index image: $CBF_{index} = \frac{M_{ctr} - M_{lbl}}{M_0}$. The perfusion index maps were co-registered and normalized to a mouse brain template [27], resized to recover the original acquisition resolutions, and rescaled by reference to the gCBF values (from PC MRI) to obtain absolute values: $rCBF = \frac{CBF_{index} \cdot gCBF}{Mean(CBF_{index})}$. Regions of interest (ROIs) were drawn on the averaged control images to encompass the cerebellum, midbrain, isocortex, hippocampus, thalamus, hypothalamus, striatum, and olfactory area by reference to the mouse brain atlas at https://atlas.brain-map.org/ (accessed on 6, October, 2024). Voxel-wise CBF values within each ROI were averaged to estimate the corresponding perfusion levels.

For each TRUST dataset, subtraction between the control and labeled images was performed to obtain different images [17]. An ROI was manually drawn on the difference image to encompass the confluence of sinuses. Four voxels exhibiting the highest difference signals were automatically selected for spatial averaging. Venous blood signal intensities at different eTE values were fitted into a monoexponential function to obtain venous T_2. Finally, T_2 was converted into Y_v using a T_2-Y_v calibration plot reported by Li and coworkers [28].

$CMRO_2$ was computed from gCBF and Y_v using the Fick principle [19], i.e., $CMRO_2 = C_a \cdot (Y_a - Y_v) \cdot gCBF$, where C_a denotes the molar concentration of oxygen in a unit volume of blood and was assumed to be 882.1 μmol O_2/100 mL blood based on previous literature [29] and Y_a was assumed to be 0.99 [30]. $CMRO_2$ was written in the unit of μmol oxygen per 100 g of brain tissue per min (μmol O_2/100 g/min).

Analogous to the pCASL data processing, ADC maps were co-registered and normalized to the brain template. ROIs were drawn on the averaged M_0 images to estimate regional ADC values.

ImageJ (National Institute of Health, USA) was used to quantify the percentage area of $CD31^+$ in different brain regions [2,8]. The scales were set based on known dimensions within the microscope images. ROIs, including the cortex, hippocampus, striatum, and olfactory area, were labeled by referring to the mouse brain atlas consistently across all microscope images. For each ROI, images were displayed in grayscale, and a threshold value was applied to isolate $CD31^+$ positive regions. The "Measure" function was then used to calculate the "% Area" of $CD31^+$ staining for each region. To assess pericyte coverage, CD13 and CD31 channels were processed with the "colocalization 2" plugin in ImageJ, which calculates the degree of overlap between the two markers. Colocalization thresholds were applied to isolate and quantify areas where $CD13^+$ pericytes were close to or overlapped with $CD31^+$ endothelial structures. The plugin provided an output metric indicating the colocalized area as a percentage of the $CD31^+$ area, representing pericyte coverage.

2.5. Statistical Analyses

An unpaired Student's *t*-test was used to assess group-wise differences in brain volume, hematocrit, and ADC, and reported with *t*-statistics and degree of freedom (DF) in the format of *t*(DF). A linear regression model was applied to examine the group effects in functional measurements (OEF, gCBF, rCBF, and $CMRO_2$), including respiration rate and heart rate as co-variates. These vital signs were used as markers to evaluate variations in anesthetic depths across the mice [25,31]. When presenting effect estimates, the coefficients of effect and 95% confidence intervals (CI) were provided. A *p* value of <0.05 was considered statistically significant, and non-significant differences were marked with n.s.

3. Results

3.1. Vascular Dysfunction in Pdgfb^{cTG} Mice

Brain volume was not significantly different between WT and $Pdgfb^{cTG}$ mice (Figure 2A, $t(8) = -0.380$, $p = 0.713$), suggesting the absence of brain atrophy or swelling. Figure 2B shows the velocity maps of PC MRI. The $Pdgfb^{cTG}$ mouse exhibited reduced blood-flow velocity or arterial area in its major feeding arteries. At the group

level, Pdgfb^{cTG} mice had significantly reduced gCBF (Figure 2C, coefficient = −72.5 mL/100 g/min, CI = [−132.7, −12.4], p = 0.025). Based on the perfusion maps obtained from pCASL (Figure 2D), we confirmed the existence of regional vulnerability to perfusion deficiency. There was no significant rCBF impairment in the cerebellum (Figure 2E, coefficient = −61.8 mL/100 g/min, CI = [−143.5, 19.9], p = 0.113), midbrain (Figure 2F, coefficient = −107.3 mL/100 g/min, CI = [−222.7, 8.1], p = 0.063), isocortex (Figure 2G, coefficient = −73.035 mL/100 g/min, CI = [−161.1, 15.0], p = 0.088), hippocampus (Figure 2H, coefficient = −18.6 mL/100 g/min, CI = [−112.0, 74.7], p = 0.642), thalamus (Figure 2I, coefficient = −35.6 mL/100 g/min, CI = [−112.3, 41.2], p = 0.300), or hypothalamus (Figure 2J, coefficient = −43.203 mL/100 g/min, CI = [−130.8, 44.4], p = 0.273). In contrast, rCBF was significantly impaired in the striatum (Figure 2K, coefficient = −89.8 mL/100 g/min, CI = [−137.5, −42.1], p = 0.004) and olfactory area (Figure 2L, coefficient = −66.2 mL/100 g/min, CI = [−123.8, −8.5], p = 0.031).

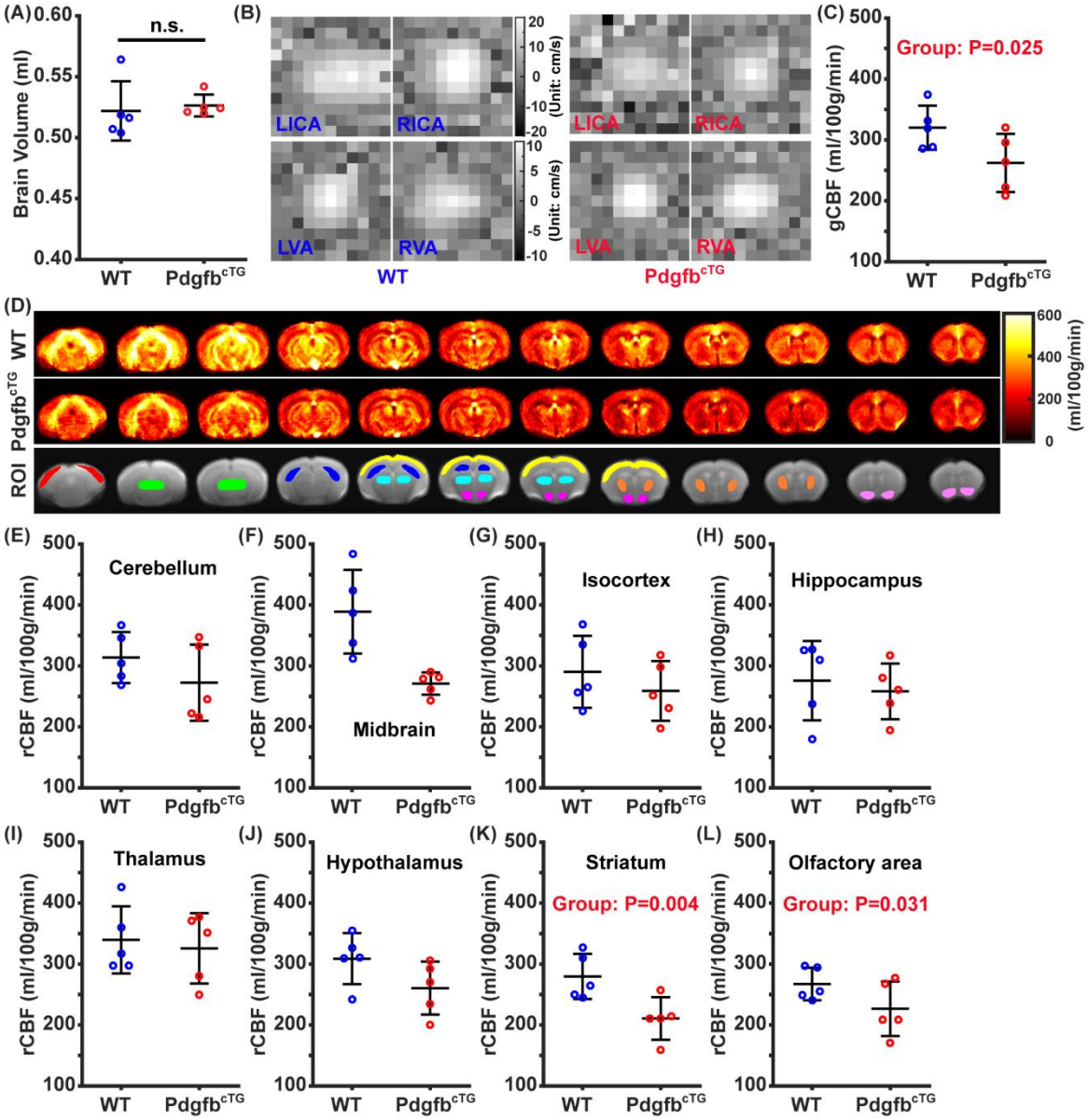

Figure 2. Comparisons of vascular function between WT and Pdgfb^{cTG} mice: (**A**) brain volume, (**B**) velocity maps of PC MRI, (**C**) gCBF, (**D**) averaged regional perfusion maps obtained using pCASL MRI with ROIs overlaid on the averaged control image, (**E**) cerebellar rCBF, (**F**) midbrain rCBF, (**G**) isocortical rCBF, (**H**) hippocampal rCBF, (**I**) thalamic rCBF, (**J**) hypothalamic rCBF, (**K**) striatal rCBF, and (**L**) olfactory rCBF.

As shown above, normalization was performed using PC-based gCBF values to provide rCBF maps with absolute values. To confirm that the normalization did not affect the statistical findings, we further analyzed the pCASL data without normalization, yielding consistent results. There was significant rCBF impairment in the striatum (Supplementary Figure S1H, coefficient = −1.07%, CI = [−2.00, −0.13], p = 0.031) and olfactory area

(Supplementary Figure S1I, coefficient = −0.80%, CI = [−1.52, −0.08], p = 0.034), but no significant impairment in other brain regions (see Supplementary Figure S1).

3.2. Metabolic Dysfunction in Pdgfb^{cTG} Mice

Figure 3A,B show the representative TRUST images of WT and Pdgfb^{cTG} mice. Difference images were obtained by pair-wise subtraction between control and labeled images. Venous signals at the confluence of sagittal sinuses were fitted and converted into Y_v using the T_2-Y_v calibration plot reported by Li et al. (Figure 3C) [28]. Pdgfb^{cTG} mice exhibited significantly higher OEF (Figure 3D, coefficient = 6.7%, CI = [3.5, 9.9], p = 0.002) and $CMRO_2$ (Figure 3E, coefficient = 80.5 µmol/100 g/min, CI = [7.9, 153.1], p = 0.035). Since hematocrit levels can be a potential confounding factor for T_2-based oxygenation measurements [32], we measured hemoglobin levels and found no significant difference (Figure 3F, $t(8)$ = 1.43, p = 0.191). Therefore, elevated OEF and $CMRO_2$ are more likely consequences of metabolic perturbation rather than hematopathy.

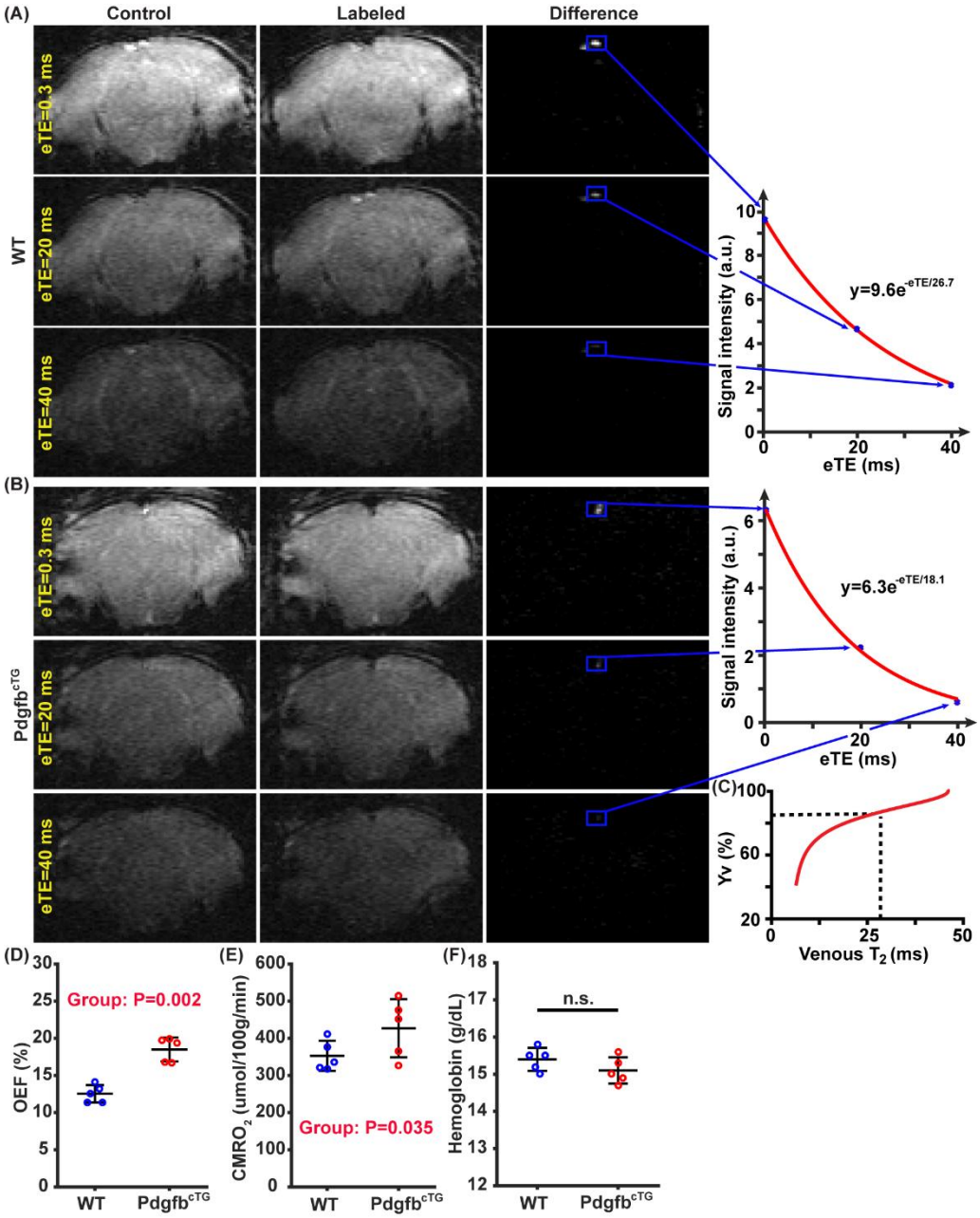

Figure 3. Comparison of brain metabolism between WT and Pdgfb^{cTG} mice. (**A**,**B**) show representative TRUST images (control, labeled, and difference) at different effective TE (0.3, 20, and 40 ms) for WT and Pdgfb^{cTG} mice, respectively. (**C**) shows the T_2-Y_v calibration curve reported by Li et al. (NMR Biomed 2020; 33: e4207). (**D**–**F**) present the comparisons of OEF, $CMRO_2$, and hemoglobin levels, respectively.

3.3. Characterizations of Diffusion Properties in the Pdgfb^{cTG} Model

Regional ADC maps were compared between WT and Pdgfb^{cTG} mice (Figure 4A). A significant difference was observed in the olfactory area (Figure 4B, $t(8) = 2.88$, $p = 0.021$), but not in other regions (Figure 4B, $|t(8)| \leq 1.99$, $p \geq 0.082$). Additionally, quantitative relaxation measurements (T_2 and T_1) were compared between the WT and Pdgfb^{cTG} mice with no significant differences observed in the cortex, hippocampus, thalamus, and hypothalamus (Supplementary Figure S2).

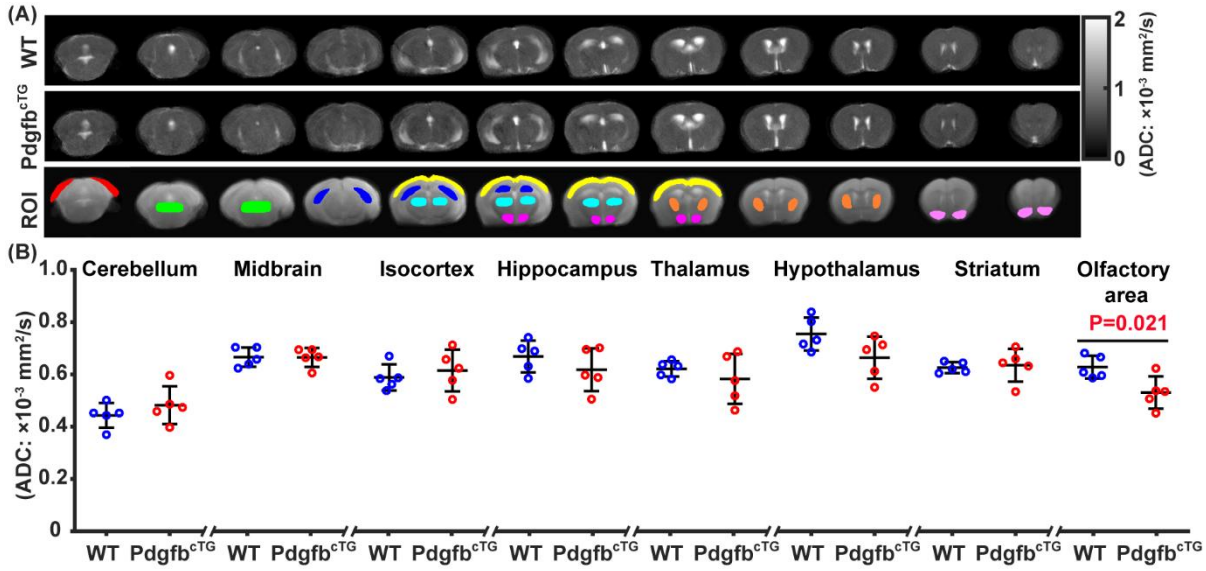

Figure 4. Comparison of microstructural features between WT and Pdgfb^{cTG} mice. (**A**) shows averaged ADC maps for WT and Pdgfb^{cTG} groups, along with corresponding ROIs. (**B**) presents regional comparisons of ADC between WT and Pdgfb^{cTG} mice.

Analysis of the diffusion and relaxation properties revealed that the Pdgfb^{cTG} mice did not develop significant microstructural abnormalities in major brain regions of the parietal lobe. Additionally, abnormal diffusion features were seen in the olfactory area of the frontal lobe in Pdgfb^{cTG} mice.

3.4. Abnormalities of Vessel Density and Pericyte Coverage in Pdgfb^{cTG} Mice

Figure 5 summarizes the results of immunofluorescence staining displaying the vessel density (CD31$^+$/region area) and pericyte coverage (CD13$^+$/CD31$^+$). Representative microscope images of WT and Pdgfb^{cTG} mice exhibited similar qualities (Figure 5A–D). Zoomed-in images in Figure 5A–D reveal tight attachment of CD13$^+$ pericytes to CD31$^+$ vascular endothelial cells across all regions in WT mice, indicating significant pericyte coverage of the capillaries (white arrows in Figure 5A–D). In contrast, many CD13$^+$ pericytes in Pdgfb^{cTG} mice were detached from the CD31$^+$ vessels in the cortex, hippocampus, and olfactory area (yellow arrows in Figure 5A,B,D). At the group level, vessel densities were preserved in the cortex (Figure 5E, $t(4) = 1.33$, $p = 0.253$) and striatum (Figure 5I, DF = 4, $t = 0.89$, $p = 0.426$), but reduced in the hippocampus (Figure 5G, $t(4) = 2.82$, $p = 0.048$) and olfactory area (Figure 5K, $t(4) = 3.78$, $p = 0.019$). Meanwhile, pericyte coverages were significantly altered in the cortex (Figure 5F, $t(4) = 3.90$, $p = 0.018$), hippocampus (Figure 5H, $t(4) = 4.45$, $p = 0.011$), and olfactory area (Figure 5L, $t(4) = 2.95$, $p = 0.042$), but not in the striatum (Figure 5J, $t(4) = -0.37$, $p = 0.727$).

The cortex exhibited normal vessel density and rCBF, but reduced pericyte coverage, implying that pericyte coverage impairment alone could not cause perfusion deficiency. Moreover, the simultaneous loss of vessel and pericyte coverage failed to induce rCBF deficiency, as evidenced by the reduced vessel density and pericyte coverage in the hippocampus, accompanied by unchanged rCBF. In contrast, the striatum, which displayed no abnormalities in vessel density or pericyte coverage, showed reduced rCBF, suggesting that impairment of vessel density or pericyte coverage is not necessary to induce perfusion deficiency.

These results indicate that regional perfusion is independent of vessel density or pericyte coverage, despite vessels being the primary structure for blood flow and pericytes regulating this flow [33]. This may be explained by the existence of compensatory mechanisms [34–36], which makes it difficult to explore the relationship between microscopic structure and macroscopic neurofunction.

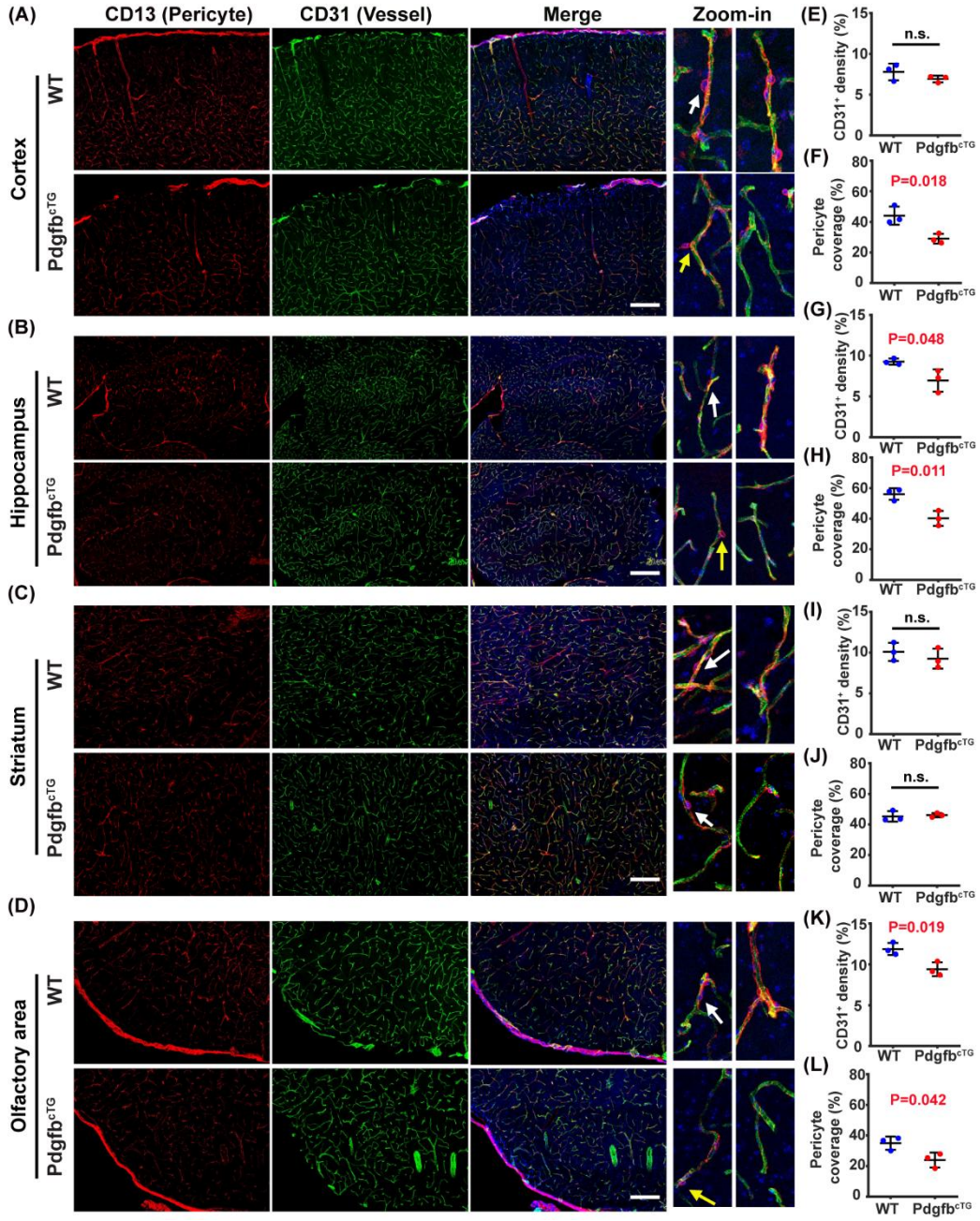

Figure 5. Analysis of immunofluorescence staining results between WT and Pdgfb^{cTG} mice. (**A**–**D**) show representative microscope images from the cortex, hippocampus, striatum, and olfactory area, respectively. The scale bar corresponds to 200 μm. Zoomed-in images (right two panels) highlight the co-localization of CD13 and CD31. White arrows indicate normal pericytes in different regions, while yellow arrows point to detached pericytes in the cortex, hippocampus, and olfactory area of Pdgfb^{cTG} mice. The ratio of the CD31^{+} area to the total regional area indicated the vessel density. Pericyte coverage was quantified as the ratio of the CD13^{+} area to the CD31^{+} area. (**E**,**G**,**I**,**K**) show the analysis of vessel density in the cortex, hippocampus, striatum, and olfactory area, respectively. (**F**,**H**,**J**,**L**) show comparisons of pericyte coverage in the cortex, hippocampus, striatum, and olfactory area, respectively.

4. Discussion

In this study, we characterized the microvascular responses to elevated circulating PDGF-BB using the Pdgfb^{cTG} mouse model through multiparametric and multimodal techniques. There were significant vascular and metabolic alterations in the Pdgfb^{cTG} mice, coupled with pathological abnormalities in vessel density and pericyte coverage. These findings extend our understanding of the effect of elevated circulating PDGF-BB on neurofunction.

Pdgfb^{cTG} mice are preosteoclast-specific *Pdgfb* transgenic mice with markedly high serum PDGF-BB concentrations from 1.5 months of age [8]. PDGF-BB, produced by preosteoclasts in bone, can promote age-

associated vascular impairment in the hippocampus, and the Pdgfb^{cTG} mice accurately replicate age-associated BBB dysfunction in the hippocampus and subsequent cognitive decline [8]. In this study, we confirmed that Pdgfb^{cTG} mice developed vascular and metabolic dysfunctions. These findings support a unique association between bone aging and cerebrovascular disorders.

Perfusion imaging revealed impaired CBF in the striatum and olfactory area, but not in other regions. This selective vulnerability to CBF impairment may be attributed to region-specific vascular characteristics, responses to elevated PDGF-BB, and compensatory mechanisms. Different brain regions have varying vessel densities [37], which may underlie their diversified vulnerability to CBF impairment. The expression of PDGF receptors, which can influence the local response to elevated PDGF-BB, may also vary across brain regions [38]. The hippocampus receives a mixed blood supply, which enhances the stability and reliability of its circulation [39]. In contrast, the striatum and olfactory area may lack such a compensatory mechanism, making them more vulnerable to vascular dysfunction. These factors, either alone or in combination, could contribute to the selective vulnerability to CBF impairment. Additionally, selective vulnerability to ADC impairment was observed. According to the literature [40], the PDGF B-chain protein exhibits the strongest expression in the olfactory system, particularly in olfactory nerve fibers, and remains at high levels in this region. The ADC impairment in the olfactory area following elevated circulating PDGF-BB may be caused by the elevated levels of PDGF B-chain protein in the olfactory system.

According to a previous report [8], abnormally elevated circulating PDGF-BB in aged mice is associated with capillary reduction, pericyte loss, and BBB dysfunction in the hippocampus. Further experiments using transgenic mice that overexpress and knockout *Pdgfb* support the mechanistic link between PDGF-BB and hippocampal vascular impairment [8]. Moreover, prolonged exposure of brain pericytes to high concentrations of PDGF-BB upregulates matrix metalloproteinase 14 (MMP14), which promotes the ectodomain shedding of PDGFRβ from the pericyte surface. This process contributes to pericyte loss and capillary reduction. By contrast, MMP inhibitor treatment alleviates hippocampal pericyte loss and capillary reduction. These findings suggest that elevated PDGF-BB impairs hippocampal vasculature by inducing PDGFRβ shedding from pericytes, disrupting their function, and degenerating the BBB integrity [8]. Following BBB disruption, toxins may extravasate from capillaries into the surrounding tissue, leading to increased neuroinflammatory activity [12]. The observed elevation in $CMRO_2$ might reflect increased mitochondrial oxidative phosphorylation, as a mechanism to generate more ATP in response to greater metabolic demands [41]. Thereafter, the increase in OEF naturally follows as a compensatory response to the elevated $CMRO_2$, but impaired blood flow [35]. Further studies are needed to fully unravel the mechanistic relationship between hypermetabolism and elevated circulating PDGF-BB. Additionally, increased circulating PDGF-BB during aging enhances the expression of soluble PDGFRβ in the cerebrospinal fluid (CSF) [8]. As increased soluble PDGFRβ in the CSF is recognized as a marker of pericyte degeneration and BBB impairment, we believe the elevated serum PDGF-BB could also serve as a marker of BBB dysfunction. However, we did not analyze the correlation between soluble PDGFRβ in the CSF and PDGF-BB in the serum due to the technical challenges of obtaining sufficient CSF from mice. Future studies need to address this question using samples collected from larger animals or human subjects.

In the context of normal aging in humans, CBF decreases, while OEF and $CMRO_2$ increase [42–45]. CBF impairment is primarily attributed to chronic developments such as stenosis, arteriovenous malfunctions, atherosclerosis, vascular-smooth-muscle-cell loss, basement membrane thickening, and cardiac dysfunction—common vascular complications in the aging population [44]. An elevated $CMRO_2$ is believed to compensate neuronal deficiency, such as mitochondrial dysfunction [46], and/or attributed to increased glial cell activity [47]. Due to neurovascular coupling [35], an increased OEF naturally is driven by the rise in $CMRO_2$ when blood flow is reduced. A longitudinal aging study in C57BL/6 mice covering major portions of mouse lifespan (3–20 months) reported consistent changes in OEF and $CMRO_2$ [15]. In contrast, CBF increases slightly with age at a rate of 1.93 mL/100 g/min/month [15]. The discrepancy between human and mouse studies suggests two possibilities: first, CBF changes in mice are non-monotonic with a sharp decline at very advanced ages (>20 months); second, the typical mouse lifespan (2–3 years) may not be long enough to induce significant CBF deficiency. According to the longitudinal study of mouse aging, the rates of change for OEF and $CMRO_2$ are 0.20%/month and 6.70 μmol/100 g/min/month, respectively [15]. In comparison, Pdgfb^{cTG} mice exhibit much more pronounced changes: −12.08 mL/100 g/min/month for CBF, 1.12%/month for OEF, and 13.42 μmol/100 g/min/month for $CMRO_2$. The above observations indicate that the Pdgfb^{cTG} model developed enhanced vascular and metabolic aging. If vascular aging is of primary interest, Pdgfb^{cTG} mice would be more suitable for research than regular C57BL/6 mice. In the literature, the interleukin 10 (IL-10) knockout model develops vascular dysfunction, such as increased vascular stiffness and decreased vascular relaxation, at 9 months of age [48]. The dietary model of hyperhomocysteinemia, a mouse model for small vessel diseases, exhibits reduced CBF after approximately 2 months on a customized diet

[49]. Dominant mutations in $NOTCH_3$ cause cerebral autosomal dominant arteriopathy with subcortical infarcts and leukoencephalopathy (CADASIL), leading to attenuated myogenic responses, impaired cerebrovascular autoregulation, and reduced CBF by 18 months of age [50]. Our finding of reduced CBF is consistent with the results observed in these mouse models, and the $Pdgfb^{cTG}$ model presents a complementary option to existing models for vascular aging.

The results of the imaging and histological examinations indicate that impaired pericyte coverage, with or without vessel loss, is insufficient to drive CBF deficiency. The presence of compensatory mechanisms may explain the decoupling between CBF, vessel density, and pericyte coverage. In the case of vessel loss, existing cerebral arteries and arterioles can dilate in response to hypoxia or chemical mediators (e.g., nitric oxide or carbon dioxide), increasing blood flow to the affected brain regions and compensating for reduced CBF [34]. Furthermore, the BBB can adapt to regulate the transport of nutrients [36]. In response to reduced CBF, the BBB may become more permeable, allowing for faster exchange of vital substances. The compensatory mechanisms indicate the complex regulation of neurofunction. Therefore, changes in the foundational structure do not necessarily lead to changes in neurofunction, exemplifying the decoupling between structure and function. As a result, imaging-based functional measurements and histological evaluations complement each other in revealing the full landscape of disease pathophysiology. Notably, the clinical diagnoses and therapeutic evaluations are often based on symptoms and functions. For example, ischemic stroke is characterized by significantly reduced CBF, a parameter of vascular function, and the efficacy of thrombolytic therapy can be assessed by perfusion imaging to map the CBF distribution [51]. In vivo functional imaging bridges the biological mechanisms with clinical diagnoses and therapeutic evaluations. The integration of non-invasive imaging with invasive histology offers a powerful tool for multiscale characterization.

Brain physiology provides valuable information for the diagnosis, stratification, staging, and treatment monitoring of various diseases [42,52,53]. Among the physiological measurements, gCBF, rCBF, OEF, and $CMRO_2$ are promising imaging biomarkers and have been extensively used in previous studies. In a rat model of cardiac arrest, gCBF, OEF, and $CMRO_2$ recover during the acute phase after the return of spontaneous circulation (ROSC), and the extent of these recoveries at the early stage (~3 h post-ROSC) can predict neurological outcomes at a later stage (24 h post-ROSC) [54]. Moreover, the hippocampus is the most vulnerable region to cardiac arrest, and restoring of hippocampal rCBF is a priority to promote neurological recovery [55]. Beyond acute physiological perturbations (e.g., cardiac arrest), physiological measurements are highly feasibility for monitoring pathologies with slow progression. Patients with AD exhibit reduced OEF and $CMRO_2$ before brain atrophy occurs [53], and cognitively healthy carriers of the apolipoprotein E4 gene show diminished OEF independent of amyloid burden [56]. Furthermore, CBF has been confirmed as a sensitive marker for studying the co-pathogenesis of AD and sleep disruption [57].

Quantitative relaxation measurements in this study were limited to a single slice. Future studies employing fast, whole-brain quantitative T_2/T_1 mapping MRI techniques [58,59] are advocated to allow cross-validation of the observed region-specific findings by providing additional microstructural information. Moreover, in such studies, experimental imperfections, such as B_1 field inhomogeneity, compromised slice selection profiles, and suboptimal gradient performance, may affect the accuracy of quantitative relaxation measurements, requiring careful consideration. We employed non-contrast, non-invasive MRI techniques to measure in vivo brain physiology, minimizing potential confounding from invasive procedures and contrast agents. However, integrating MRI with other optical imaging methods could enhance the specificity of measurements and improve the interpretation of MRI findings [60,61]. Furthermore, NMR-based metabolomics [62,63] could provide additional molecular insights into metabolic pathway perturbations, allowing deeper understanding of the causal and consequential relationships between neurofunction and metabolites.

We performed Monte Carlo simulations (20,000 iterations) based on the collected data to assess the statistical power of this study. The simulations revealed a power of 0.83 to detect differences in gCBF, 0.99 for OEF, and 0.72 for $CMRO_2$, which are the key findings supporting the study's conclusions.

The present results should be interpreted with caution in light of the following several limitations. First, we characterized the vascular and metabolic responses to elevated circulating PDGF-BB, providing neurofunctional evidence for its pro-aging effect, no deeper mechanistic tests were performed to elucidate the underlying causal relationships at the molecular level. Second, only male mice were used in this study. According to our previous study [2], circulating PDGF-BB levels are differentially altered by age in male and female mice. Further investigations should investigate the effects of menopause on the neurofunctional profile while considering sex difference to deepen our understanding of the neurofunctional responses to elevated circulating PDGF-BB. Thirdly, our study is limited to a mouse model. Given the species difference between humans and mice, future studies in humans are advocated to validate the results of this study. It is worth noting that MRI techniques for measuring

CBF, OEF, and $CMRO_2$ are readily applicable to human scanners [23,64–66], suggesting that the clinical translation of our findings is straightforward. Additionally, the multiparametric observations conducted in this study suggest that the onset of abnormalities may occur over varying timelines. Given the cross-sectional nature of this study, we did not capture the full landscape of the multifaceted pathophysiological progression. A future study employing a longitudinal design with a larger sample size would be valuable to determine the cascade of different physiological and microstructural events over time. Therefore, the current findings serve as a guide for future mechanistic studies to determine the causal relationships between different abnormalities, thereby identifying potential therapeutic targets.

In conclusion, hypoperfusion and hypermetabolism occur as a result of elevated circulating PDGF-BB in mice. Our study provides neurofunctional evidence supporting the notion that increased circulating PDGF-BB accelerates both vascular and metabolic dysfunction in the brain.

Supplementary Materials: The following supporting information can be downloaded at: https://www.sciltp.com/journals/hm/2025/1/608/s1, Figure S1: rCBF without normalization to PC results; Figure S2: Quantitative relaxation measurements in the $Pdgfb^{cTG}$ model.

Author Contributions: X.Y.: validation, software, formal analysis, visualization, writing—original draft; J.W.: investigation, validation, formal analysis, visualization, writing—original draft; Y.L.: investigation; writing—review & editing; M.W.: conceptualization, methodology, resources, supervision, funding acquisition, writing—review & editing; Z.W.: conceptualization, methodology, resources, data curation, supervision, funding acquisition, writing—review & editing. All authors have read and agreed to the published version of the manuscript.

Funding: This work was supported by the National Institute of Health under R21 NS119960, R01 AG081932, R01AG072090, and P41 EB031771.

Institutional Review Board Statement: The experimental protocols involved in this study were approved by the Johns Hopkins Medical Institution Animal Care and Use Committee and conducted in accordance with the National Institutes of Health guidelines for the care and use of laboratory animals.

Informed Consent Statement: Not applicable.

Data Availability Statement: MRI and immunofluorescent staining data reported in this work are available upon request.

Conflicts of Interest: The author(s) declared no potential conflicts of interest with respect to the research, authorship, and/or publication of this article.

References

1. Santhanam, L.; Liu, G.; Jandu, S.; Su, W.; Wodu, B.P.; Savage, W.; Poe, A.; Liu, X.; Alexander, L.M.; Cao, X.; et al. Skeleton-secreted PDGF-BB mediates arterial stiffening. *J. Clin. Investig.* **2021,** *131*, e147116.
2. Wang, J.; Fang, C.L.; Noller, K.; Wei, Z.; Liu, G.; Shen, K.; Song, K.; Cao, X.; Wan, M. Bone-derived PDGF-BB drives brain vascular calcification in male mice. *J. Clin. Investig.* **2023,** *133*, e168447.
3. Mitlak, B.H.; Finkelman, R.D.; Hill, E.L.; Li, J.; Martin, B.; Smith, T.; D'Andrea, M.; Antoniades, H.N.; Lynch, S.E. The effect of systemically administered PDGF-BB on the rodent skeleton. *J. Bone Miner. Res.* **1996,** *11*, 238–247.
4. Lindahl, P.; Johansson, B.R.; Levéen, P.; Betsholtz, C. Pericyte loss and microaneurysm formation in PDGF-B-deficient mice. *Science* **1997,** *277*, 242–245.
5. Hellström, M.; Kalén, M.; Lindahl, P.; Abramsson, A.; Betsholtz, C. Role of PDGF-B and PDGFR-beta in recruitment of vascular smooth muscle cells and pericytes during embryonic blood vessel formation in the mouse. *Development* **1999,** *126*, 3047–3055.
6. Cicognola, C.; Mattsson-Carlgren, N.; van Westen, D.; Zetterberg, H.; Blennow, K.; Palmqvist, S.; Ahmadi, K.; Strandberg, O.; Stomrud, E.; Janelidze, S.; et al. Associations of CSF PDGFRβ with aging, blood-brain barrier damage, neuroinflammation, and Alzheimer disease pathologic changes. *Neurology* **2023,** *101*, e30–e39.
7. Butts, B.; Huang, H.; Hu, W.T.; Kehoe, P.G.; Miners, J.S.; Verble, D.D.; Zetterberg, H.; Zhao, L.; Trotti, L.M.; Benameur, K.; et al. sPDGFRβ and neuroinflammation are associated with AD biomarkers and differ by race: The ASCEND study. *Alzheimers Dement.* **2024,** *20*, 1175–1189.
8. Liu, G.; Wang, J.; Wei, Z.; Fang, C.L.; Shen, K.; Qian, C.; Qi, C.; Li, T.; Gao, P.; Wong, P.C.; et al. Elevated PDGF-BB from bone impairs hippocampal vasculature by inducing PDGFRβ shedding from pericytes. *Adv. Sci.* **2023,** *10*, e2206938.
9. Kapoor, A.; Nation, D.A. Platelet-derived growth factor-BB and white matter hyperintensity burden in APOE4 carriers. *Cereb. Circ. Cogn. Behav.* **2022,** *3*, 100131.
10. Smyth, L.C.D.; Highet, B.; Jansson, D.; Wu, J.; Rustenhoven, J.; Aalderink, M.; Tan, A.; Li, S.; Johnson, R.; Coppieters, N.; et al. Characterisation of PDGF-BB:PDGFRβ signalling pathways in human brain pericytes: Evidence of disruption in Alzheimer's disease. *Commun. Biol.* **2022,** *5*, 235.

11. Gianni, D.; Zambrano, N.; Bimonte, M.; Minopoli, G.; Mercken, L.; Talamo, F.; Scaloni, A.; Russo, T. Platelet-derived growth factor induces the beta-gamma-secretase-mediated cleavage of Alzheimer's amyloid precursor protein through a Src-Rac-dependent pathway. *J. Biol. Chem.* **2003,** *278*, 9290–9297.
12. Liu, G.; Shu, W.; Chen, Y.; Fu, Y.; Fang, S.; Zheng, H.; Cheng, W.; Lin, Q.; Hu, Y.; Jiang, N.; et al. Bone-derived PDGF-BB enhances hippocampal non-specific transcytosis through microglia-endothelial crosstalk in HFD-induced metabolic syndrome. *J. Neuroinflamm.* **2024,** *21*, 111.
13. Fang, C.L.; Liu, B.; Wan, M. "Bone-SASP" in skeletal aging. *Calcif. Tissue Int.* **2023,** *113*, 68–82.
14. Wei, Z.; Xu, J.; Chen, L.; Hirschler, L.; Barbier, E.L.; Li, T.; Wong, P.C.; Lu, H. Brain metabolism in tau and amyloid mouse models of Alzheimer's disease: An MRI study. *NMR Biomed.* **2021,** *34*, e4568.
15. Wei, Z.; Chen, L.; Hou, X.; van Zijl, P.C.M.; Xu, J.; Lu, H. Age-related alterations in brain perfusion, venous oxygenation, and oxygen metabolic rate of mice: A 17-month longitudinal MRI study. *Front. Neurol.* **2020,** *11*, 559.
16. Wei, Z.; Chen, L.; Lin, Z.; Jiang, D.; Xu, J.; Liu, P.; van Zijl, P.C.M.; Lu, H. Optimization of phase-contrast MRI for the estimation of global cerebral blood flow of mice at 11.7T. *Magn. Reson. Med.* **2019,** *81*, 2566–2575.
17. Wei, Z.; Xu, J.; Liu, P.; Chen, L.; Li, W.; van Zijl, P.C.M.; Lu, H. Quantitative assessment of cerebral venous blood T2 in mouse at 11.7T: Implementation, optimization, and age effect. *Magn. Reson. Med.* **2018,** *80*, 521–528.
18. Hirschler, L.; Debacker, C.S.; Voiron, J.; Kohler, S.; Warnking, J.M.; Barbier, E.L. Interpulse phase corrections for unbalanced pseudo-continuous arterial spin labeling at high magnetic field. *Magn. Reson. Med.* **2018,** *79*, 1314–1324.
19. Kety, S.S.; Schmidt, C.F. The nitrous oxide method for the quantitative determination of cerebral blood flow in man: Theory, procedure and normal values. *J. Clin. Investig.* **1948,** *27*, 476–483.
20. Pires Monteiro, S.; Hirschler, L.; Barbier, E.L.; Figueiredo, P.; Shemesh, N. High-resolution perfusion imaging in rodents using pCASL at 9.4 T. *bioRxiv* **2024**, bioRxiv:03.07.583839.
21. Wei, Z.; Li, Y.; Hou, X.; Han, Z.; Xu, J.; McMahon, M.T.; Duan, W.; Liu, G.; Lu, H. Quantitative cerebrovascular reactivity MRI in mice using acetazolamide challenge. *Magn. Reson. Med.* **2022,** *88*, 2233–2241.
22. Wei, Z.; Liu, H.; Lin, Z.; Yao, M.; Li, R.; Liu, C.; Li, Y.; Xu, J.; Duan, W.; Lu, H. Non-contrast assessment of blood-brain barrier permeability to water in mice: An arterial spin labeling study at cerebral veins. *Neuroimage* **2023,** *268*, 119870.
23. Lu, H.; Ge, Y. Quantitative evaluation of oxygenation in venous vessels using T2-Relaxation-Under-Spin-Tagging MRI. *Magn. Reson. Med.* **2008,** *60*, 357–363.
24. Yang, X. Improving the reliability of T2 measurement in magnetic resonance imaging. *bioRxiv* **2024**, bioRxiv:06.09.598128.
25. Wei, Z.; Roh, S.E.; Yang, X.; Wang, W.; Wang, J.; Chen, L.; Li, Y.; Bibic, A.; Lu, H. The impact of isoflurane anesthesia on brain metabolism in mice: An MRI and electroencephalography (EEG) study. *NMR Biomed.* **2024,** *37*, e5260.
26. Leithner, C.; Muller, S.; Fuchtemeier, M.; Lindauer, U.; Dirnagl, U.; Royl, G. Determination of the brain-blood partition coefficient for water in mice using MRI. *J. Cereb. Blood Flow Metab.* **2010,** *30*, 1821–1824.
27. Meyer, C.E.; Kurth, F.; Lepore, S.; Gao, J.L.; Johnsonbaugh, H.; Oberoi, M.R.; Sawiak, S.J.; MacKenzie-Graham, A. In vivo magnetic resonance images reveal neuroanatomical sex differences through the application of voxel-based morphometry in C57BL/6 mice. *Neuroimage* **2017,** *163*, 197–205.
28. Li, W.; van Zijl, P.C.M. Quantitative theory for the transverse relaxation time of blood water. *NMR Biomed.* **2020,** *33*, e4207.
29. Ulatowski, J.A.; Oja, J.M.E.; Suarez, J.I.; Kauppinen, R.A.; Traystman, R.J.; van Zijl, P.C.M. In vivo determination of absolute cerebral blood volume using hemoglobin as a natural contrast agent: An MRI study using altered arterial carbon dioxide tension. *J. Cereb. Blood Flow Metab.* **1999,** *19*, 809–817.
30. Lin, A.L.; Qin, Q.; Zhao, X.; Duong, T.Q. Blood longitudinal (T1) and transverse (T2) relaxation time constants at 11.7 Tesla. *Magn. Reson. Mater.Phys. Biol. Med.* **2012,** *25*, 245–249.
31. Wei, Z.; Li, Y.; Bibic, A.; Duan, W.; Xu, J.; Lu, H. Toward accurate cerebral blood flow estimation in mice after accounting for anesthesia. *Front. Physiol.* **2023,** *14*, 1169622.
32. Lu, H.; Xu, F.; Grgac, K.; Liu, P.; Qin, Q.; van Zijl, P. Calibration and validation of TRUST MRI for the estimation of cerebral blood oxygenation. *Magn. Reson. Med.* **2012,** *67*, 42–49.
33. Hall, C.N.; Reynell, C.; Gesslein, B.; Hamilton, N.B.; Mishra, A.; Sutherland, B.A.; O'Farrell, F.M.; Buchan, A.M.; Lauritzen, M.; Attwell, D. Capillary pericytes regulate cerebral blood flow in health and disease. *Nature* **2014,** *508*, 55–60.
34. Faraci, F.M.; Breese, K.R.; Heistad, D.D. Cerebral vasodilation during hypercapnia. Role of glibenclamide-sensitive potassium channels and nitric oxide. *Stroke* **1994,** *25*, 1679–1683.
35. Peterson, E.C.; Wang, Z.; Britz, G. Regulation of cerebral blood flow. *Int. J. Vasc. Med.* **2011,** *2011*, 823525.
36. Segarra, M.; Aburto, M.R.; Acker-Palmer, A. Blood-brain barrier dynamics to maintain brain homeostasis. *Trends Neurosci.* **2021,** *44*, 393–405.

37. Xiong, B.; Li, A.; Lou, Y.; Chen, S.; Long, B.; Peng, J.; Yang, Z.; Xu, T.; Yang, X.; Li, X.; et al. Precise cerebral vascular atlas in stereotaxic coordinates of whole mouse brain. *Front. Neuroanat.* **2017,** *11*, 128.
38. Winkler, E.A.; Bell, R.D.; Zlokovic, B.V. Pericyte-specific expression of PDGF beta receptor in mouse models with normal and deficient PDGF beta receptor signaling. *Mol. Neurodegener.* **2010,** *5*, 32.
39. Perosa, V.; Priester, A.; Ziegler, G.; Cardenas-Blanco, A.; Dobisch, L.; Spallazzi, M.; Assmann, A.; Maass, A.; Speck, O.; Oltmer, J.; et al. Hippocampal vascular reserve associated with cognitive performance and hippocampal volume. *Brain* **2020,** *143*, 622–634.
40. Heldin, C.H.; Westermark, B. Mechanism of action and in vivo role of platelet-derived growth factor. *Physiol. Rev.* **1999,** *79*, 1283–1316.
41. Smeitink, J.; van den Heuvel, L.; DiMauro, S. The genetics and pathology of oxidative phosphorylation. *Nat. Rev. Genet.* **2001,** *2*, 342–352.
42. Lu, H.; Xu, F.; Rodrigue, K.M.; Kennedy, K.M.; Cheng, Y.; Flicker, B.; Hebrank, A.C.; Uh, J.; Park, D.C. Alterations in cerebral metabolic rate and blood supply across the adult lifespan. *Cereb. Cortex.* **2011,** *21*, 1426–1634.
43. Deery, H.A.; Liang, E.; Di Paolo, R.; Voigt, K.; Murray, G.; Siddiqui, M.N.; Egan, G.F.; Moran, C.; Jamadar, S.D. The association of regional cerebral blood flow and glucose metabolism in normative ageing and insulin resistance. *Sci. Rep.* **2024,** *14*, 14574.
44. Nagata, K.; Yamazaki, T.; Takano, D.; Maeda, T.; Fujimaki, Y.; Nakase, T.; Sato, Y. Cerebral circulation in aging. *Ageing Res. Rev.* **2016,** *30*, 49–60.
45. Peng, S.L.; Dumas, J.A.; Park, D.C.; Liu, P.; Filbey, F.M.; McAdams, C.J.; Pinkham, A.E.; Adinoff, B.; Zhang, R.; Lu, H. Age-related increase of resting metabolic rate in the human brain. *Neuroimage* **2014,** *98*, 176–183.
46. Amorim, J.A.; Coppotelli, G.; Rolo, A.P.; Palmeira, C.M.; Ross, J.M.; Sinclair, D.A. Mitochondrial and metabolic dysfunction in ageing and age-related diseases. *Nat. Rev. Endocrinol.* **2022,** *18*, 243–258.
47. Yin, F.; Sancheti, H.; Patil, I.; Cadenas, E. Energy metabolism and inflammation in brain aging and Alzheimer's disease. *Free Radic. Biol. Med.* **2016,** *100*, 108–122.
48. Sikka, G.; Miller, K.L.; Steppan, J.; Pandey, D.; Jung, S.M.; Fraser, C.D., 3rd; Ellis, C.; Ross, D.; Vandegaer, K.; Bedja, D.; et al. Interleukin 10 knockout frail mice develop cardiac and vascular dysfunction with increased age. *Exp. Gerontol.* **2013,** *48*, 128–135.
49. Braun, D.J.; Abner, E.; Bakshi, V.; Goulding, D.S.; Grau, E.M.; Lin, A.L.; Norris, C.M.; Sudduth, T.L.; Webster, S.J.; Wilcock, D.M.; et al. Blood flow deficits and cerebrovascular changes in a dietary model of hyperhomocysteinemia. *ASN Neuro* **2019,** *11*, 1–13.
50. Joutel, A.; Monet-Lepretre, M.; Gosele, C.; Baron-Menguy, C.; Hammes, A.; Schmidt, S.; Lemaire-Carrette, B.; Domenga, V.; Schedl, A.; Lacombe, P.; et al. Cerebrovascular dysfunction and microcirculation rarefaction precede white matter lesions in a mouse genetic model of cerebral ischemic small vessel disease. *J. Clin. Investig.* **2010,** *120*, 433–445.
51. Ma, H.; Campbell, B.C.V.; Parsons, M.W.; Churilov, L.; Levi, C.R.; Hsu, C.; Kleinig, T.J.; Wijeratne, T.; Curtze, S.; Dewey, H.M.; et al. Thrombolysis guided by perfusion imaging up to 9 h after onset of stroke. *N. Engl. J. Med.* **2019,** *380*, 1795–1803.
52. Shetty, A.N.; Lucke, A.M.; Liu, P.; Sanz Cortes, M.; Hagan, J.L.; Chu, Z.D.; Hunter, J.V.; Lu, H.; Lee, W.; Kaiser, J.R. Cerebral oxygen metabolism during and after therapeutic hypothermia in neonatal hypoxic-ischemic encephalopathy: A feasibility study using magnetic resonance imaging. *Pediatr. Radiol.* **2019,** *49*, 224–233.
53. Thomas, B.P.; Sheng, M.; Tseng, B.Y.; Tarumi, T.; Martin-Cook, K.; Womack, K.B.; Cullum, M.C.; Levine, B.D.; Zhang, R.; Lu, H. Reduced global brain metabolism but maintained vascular function in amnestic mild cognitive impairment. *J. Cereb. Blood Flow Metab.* **2017,** *37*, 1508–1516.
54. Wei, Z.; Wang, Q.; Modi, H.R.; Cho, S.-M.; Geocadin, R.G.; Thakor, N.V.; Lu, H. Acute-stage MRI cerebral oxygen consumption biomarkers predict 24-h neurological outcome in a rat cardiac arrest model. *NMR Biomed.* **2020,** *33*, e4377.
55. Guo, Y.; Cho, S.-M.; Wei, Z.; Wang, Q.; Modi, H.R.; Gharibani, P.; Lu, H.; Thakor, N.V.; Geocadin, R.G. Early thalamocortical reperfusion leads to neurologic recovery in a rodent cardiac arrest model. *Neurocrit. Care* **2022,** *37*, 60–72.
56. Lin, Z.; Sur, S.; Soldan, A.; Pettigrew, C.; Miller, M.; Oishi, K.; Bilgel, M.; Moghekar, A.; Pillai, J.J.; Albert, M.; et al. Brain oxygen extraction by using MRI in older individuals: Relationship to apolipoprotein E genotype and amyloid burden. *Radiology* **2019,** *292*, 140–148.
57. Han, X.; Liu, G.; Lee, S.S.; Yang, X.; Wu, M.N.; Lu, H.; Wei, Z. Metabolic and vascular imaging markers for investigating Alzheimer's disease complicated by sleep fragmentation in mice. *Front. Physiol.* **2024,** *15*, 1456690.
58. Li, S.; Kang, T.; Wu, J.; Chen, W.; Lin, Q.; Wu, Z.; Wang, J.; Cai, C.; Cai, S. Sub-second whole brain T(2)mapping via multiband SENSE multiple overlapping-echo detachment imaging and deep learning. *Phys. Med. Biol.* **2023,** *68*, 195027.

59. Hamilton, J.I.; Pahwa, S.; Adedigba, J.; Frankel, S.; O'Connor, G.; Thomas, R.; Walker, J.R.; Killinc, O.; Lo, W.C.; Batesole, J.; et al. Simultaneous mapping of T(1) and T(2) using cardiac magnetic resonance fingerprinting in a cohort of healthy subjects at 1.5T. *J. Magn. Reson. Imaging* **2020,** *52*, 1044–1052.
60. Ren, Y.; Chu, X.; Senarathna, J.; Bhargava, A.; Grayson, W.L.; Pathak, A.P. Multimodality imaging reveals angiogenic evolution in vivo during calvarial bone defect healing. *Angiogenesis* **2024,** *27*, 105–119.
61. Chong, S.P.; Merkle, C.W.; Leahy, C.; Srinivasan, V.J. Cerebral metabolic rate of oxygen (CMRO2) assessed by combined Doppler and spectroscopic OCT. *Biomed. Opt. Express* **2015,** *6*, 3941–3951.
62. Lin, C.; Chen, Z.; Zhang, L.; Wei, Z.; Cheng, K.-K.; Liu, Y.; Shen, G.; Fan, H.; Dong, J. Deciphering the metabolic perturbation in hepatic alveolar echinococcosis: A 1 H NMR-based metabolomics study. *Parasites Vec.* **2019,** *12*, 300.
63. Liu, X.; Zhou, Y.; Qi, Z.; Huang, C.; Lin, D. Taurine alleviates ferroptosis-induced metabolic impairments in C2C12 myoblasts by stabilizing the labile iron pool and improving redox homeostasis. *J. Proteome Res.* **2024,** *23*, 3444–3459.
64. Peng, S.L.; Su, P.; Wang, F.N.; Cao, Y.; Zhang, R.; Lu, H.; Liu, P. Optimization of phase-contrast MRI for the quantification of whole-brain cerebral blood flow. *J. Magn. Reson. Imaging* **2015,** *42*, 1126–1133.
65. Liu, P.; Xu, F.; Lu, H. Test-retest reproducibility of a rapid method to measure brain oxygen metabolism. *Magn. Reson. Med.* **2013,** *69*, 675–681.
66. Jiang, D.; Lu, H.; Parkinson, C.; Su, P.; Wei, Z.; Pan, L.; Tekes, A.; Huisman, T.A.; Golden, C.W.; Liu, P. Vessel-specific quantification of neonatal cerebral venous oxygenation. *Magn. Reson. Med.* **2019,** *82*, 1129–1139.